Dalton Transactions

ROYAL SOCIETY OF CHEMISTRY

PAPER

View Article Online
View Journal | View Issue

Cite this: *Dalton Trans.*, 2025, **54**, 13934

Advanced nitrogen-doped transition metal oxides decorated with Pt: synthesis and composition strategies for maximised electrochemical performance

Kristina Gočanin,[a] Yasemin Aykut,[b] Dušan Mladenović, *[a] Diogo M. F. Santos, [c] Ayşe Bayrakçeken, [b] Gulin S. P. Soylu [d] and Biljana Šljukić [a,c]

Received 22nd May 2025,
Accepted 26th August 2025

DOI: 10.1039/d5dt01211b

rsc.li/dalton

Developing efficient, low-cost catalysts for oxygen reduction and evolution reactions (ORR and OER) is key to advancing metal–air batteries and regenerative fuel cells. In this study, nitrogen-doped binary metal (Mn and Ni) oxides (N–BMOs) and Pt-decorated N–BMOs were synthesised using three methods and tested as ORR and OER catalysts in alkaline media. Their physicochemical properties were characterised by XRD, N_2-sorption, TEM, and XPS, while their electrochemical performance was evaluated using voltammetry and impedance spectroscopy. Among all tested materials, the best bifunctional catalyst proved to be Pt/N–Mn_2O_3–NiO (1 : 1) (S3) with the highest achieved diffusion limited current density (–4.98 mA cm^{-2} at 1800 rpm), the highest kinetic current density (–15.3 mA cm^{-2}), low Tafel slope (75 mV dec^{-1}) in ORR potential region, and overpotential of 0.56 V to reach benchmark current value of 10 mA cm^{-2} during OER. The ΔE was calculated to be 0.95 V, comparable to or even better than that of similar materials reported in the literature. Pt/N–Mn_2O_3–NiO (1 : 1) (S3) demonstrated striking stability during long-term operation with preserved morphology and catalytic activity.

Introduction

The search for alternative energy sources and viable systems for energy storage and conversion has never been more widespread than in the last few decades. Electrochemical systems, such as batteries, supercapacitors, and fuel cells, have been investigated as potential energy storage systems that can utilise energy from primary, renewable sources when available and then release the stored energy when needed. Alkaline unitised regenerative fuel cells (A-URFCs) are a type of fuel cell that can operate in both fuel cell mode and electrolysis mode.[1] In electrolysis mode, the cell produces hydrogen and oxygen, which can be stored and transported. When energy is not being supplied, the cell can switch to fuel cell mode, using the stored hydrogen and oxygen to generate electricity.[2–5] In theory, this system could operate indefinitely with much higher efficiency than batteries or supercapacitors.[1,6] However, challenges exist in designing and constructing A-URFCs, particularly due to the slow kinetics of the oxygen reduction reaction (ORR) and the complexity of having different reactions, oxygen reduction and oxygen evolution (OER) occurring on the same electrodes in two modes.[7] Additionally, platinum (Pt), traditionally considered the best catalyst for ORR, and iridium oxide (IrO_2) and ruthenium oxide (RuO_2), which are regarded as the best catalysts for oxygen evolution in the electrolysis mode, are all expensive. This has driven researchers to search for alternative catalysts made from more abundant, earth-friendly elements.

Transition metals and transition metal oxides (TMOs) have garnered significant attention from researchers due to their high natural abundance and low cost,[8] along with excellent performance in oxygen reduction and oxygen evolution reactions.[9–11] Moreover, these materials have proven to be effective carriers (*supports*) of active particles. Zhao and co-workers synthesised MOF-derived nitrogen-doped carbon nanotubes encapsulated with bimetallic oxide, FeNiO@NCNT, which reached a diffusion-limited current density, j_d, of −2.5 mA cm^{-2} at 1600 rpm with ΔE of 0.82 V.[12] Morales *et al.* synthesised trimetallic Mn–Fe–Ni oxides on multi-walled carbon nanotubes (MWCNTs) by first growing and oxygen-functionalising MWCNTs to obtain MWCNTs-Ox with an

[a]*University of Belgrade, Faculty of Physical Chemistry, Studentski trg 12-16, 11158 Belgrade, Serbia. E-mail: dusan.mladenovic@ffh.bg.ac.rs*
[b]*Department of Chemical Engineering, Atatürk University, Erzurum, 25240, Turkey*
[c]*Center of Physics and Engineering of Advanced Materials, Laboratory of Physics for Materials and Emerging Technologies, Chemical Engineering Department, Instituto Superior Técnico, Universidade de Lisboa, 1049-001 Lisbon, Portugal*
[d]*Faculty of Engineering, Chemical Engineering Department, Istanbul University-Cerrahpasa, 34320 Avcilar, Istanbul, Turkey*

average outer diameter of 8 to 10 nm. MnO_x was then incorporated into Fe–Ni oxide previously supported on MWCNTs-Ox.[13] $Mn_{0.5}(Fe_{0.3}Ni_{0.7})_{0.5}O_x$/MWCNTs-$O_x$ showed low values of ORR and OER overpotentials with the ΔE of 0.73 V and j_d in the ORR potential region of −4.2 mA cm^{-2} at 1600 rpm. Shao *et al.* synthesised carbon dots that bridge NiO and Mn_2O_3, NiO–Mn_2O_3–CDs, which showed an almost four-electron oxygen reduction (n = 3.85) and ΔE 0.72 V.[14] Furthermore, the material achieved j_d of −6 mA cm^{-2} in ORR mode and 10 mA cm^{-2} in OER mode at an overpotential of 0.298 V. In the authors' previous work, non-doped bimetallic Pt/Mn_2O_3–NiO[15] and nitrogen-doped Pt/Mn_2O_3–NiO–N[16] were synthesised and tested under the same conditions as bifunctional URFC catalysts. The undoped Pt/Mn_2O_3–NiO showed remarkable activity, achieving −4.475 mA cm^{-2} at 1800 rpm and ΔE of 1.03 V, while the Pt/Mn_2O_3–NiO–N showed ΔE values of 0.88–0.99 V and j_d of −4.43 to −4.81 mA cm^{-2}, depending on the BMO to N ratio. Though Pt might outperform TMOs, it should be kept in mind that Pt is known to undergo oxidation at higher potentials,[17] which effectively increases the ORR overpotential[17,18] and reduces the OER activity of the catalyst, unlike transition metal oxides that cannot be so easily oxidised when increasing applied potentials.[10,19,20]

This work continued the investigation of nitrogen-doped N–Mn_2O_3–NiO and Pt/N–Mn_2O_3–NiO (with 20 wt% Pt) with two different ratios of BMO to N by slightly modifying the synthesis procedure to improve the catalytic performance of the materials. Three modified procedures were used to synthesise the materials designated as (S1), (S2), and (S3), which were then tested in alkaline media as bifunctional oxygen electrode catalysts. This design is based on the synergy between the excellent catalytic activity and electrical conductivity of Pt with the tuneable surface chemistry, defect structure, and stability of N-doped BMOs. Nitrogen-doping introduces electronic modifications and surface defects that can enhance Pt anchoring, dispersion, and charge transfer kinetics. By engineering the metal–support interface and optimising particle distribution, the composite materials aim to simultaneously boost electrochemically active surface area (ECSA), reduce overpotentials for ORR and OER, and improve long-term catalytic durability. Electrochemical testing revealed significant improvements in both OER and ORR activity compared to the undoped BMO, demonstrating the effectiveness of the combined doping-deposition approach and highlighting the potential of these hybrid materials as bifunctional electrocatalysts for energy conversion systems such as metal–air batteries and regenerative fuel cells.

Experimental

Synthesis of Mn_2O_3–NiO structures

Materials. Starting materials for binary oxide preparation, $Mn(NO_3)_2{\cdot}4H_2O$ (≥98.5%, Merck), $Ni(NO_3)_2{\cdot}6H_2O$ (≥97%, Sigma-Aldrich), nickel(II) acetylacetonate (≥95%, Sigma-Aldrich), nitric acid (65%, Merck), ammonia solution (25% in water), and ethanol (absolute) were purchased from the Fluka Company and used without further purification. Deionised (D. I.) water was used for the preparation of all the oxides.

The co-precipitation synthesis of Mn_2O_3–NiO binary oxide (S1). Mn_2O_3–NiO powders were prepared by the co-precipitation method. The typical steps were as follows: 0.015 mol $Mn(NO_3)_3{\cdot}4H_2O$ and 0.015 mol $Ni(NO_3)_2{\cdot}6H_2O$ were dissolved in 150 mL of 2 M HNO_3 solution separately, and each was stirred for 0.5 h at room temperature. After that, the two mixtures were combined in a 1 : 1 molar ratio and stirred for approximately 1 h. This mixture was precipitated by gradually adding NH_3 solution (25 wt%) until the pH value reached 13. The resultant solution was slowly stirred at 70 °C for 2 h. The resulting precipitate was separated by filtration and sequentially washed with ultrapure water and ethanol to remove NO_3^- anions. Finally, the precipitate was dried at 80 °C for 12 h and calcinated at 450 °C for 4 h. The resultant Mn_2O_3–NiO powders were ground at a constant vibration rate of 300 rpm for 10 min in a Retsch MM 200 vibratory ball mill.

The co-precipitation synthesis of Mn_2O_3–NiO binary oxide (S2). Mn_2O_3–NiO powders were prepared by the co-precipitation method. The typical steps were as follows: 0.015 mol $Mn(NO_3)_3{\cdot}4H_2O$ and 0.015 mol $Ni(NO_3)_2{\cdot}6H_2O$ were dissolved in 150 mL of warm deionised water separately, and each was stirred for 0.5 h at 45 °C in an ultrasonic bath. After that, the two mixtures were combined in a 1 : 1 molar ratio. This mixture was precipitated by gradually adding NH_3 solution (25 wt%) until the pH value reached 11. The resultant solution was slowly stirred at 75 °C for 5 h. The resulting precipitate was separated by filtration and sequentially washed with ultrapure water and ethanol to remove NO_3^- anions. Finally, the precipitate was dried at 80 °C for 12 h and calcinated at 450 °C for 4 h. The resultant Mn_2O_3–NiO powders were ground at a constant vibration rate of 300 rpm for 10 min in a Retsch MM200 vibratory ball mill.

The solid-state preparation of binary metal oxides (S3). NiO was prepared by the co-precipitation method. An appropriate amount of metal nitrate ($Ni(NO_3)_2{\cdot}6H_2O$) was dissolved in deionised warm water, and the resulting solution was heated to 65 °C. This mixture was precipitated by gradually adding NH_3 solution (25 wt%) until the pH value reached 10. The resultant solution was slowly stirred for 2 h at 65 °C. After that, the solution was irradiated under 600 W microwave for 3 min. The precipitate was then filtered, washed with deionised water, and dried at 110 °C for 20 h and calcined at 500 °C for 3 h.

Mn_2O_3 was prepared by co-precipitation. An appropriate amount of metal nitrate ($Mn(NO_3)_2{\cdot}4H_2O$) was dissolved in deionised warm water, and the resulting solution was heated to 65 °C. This mixture was precipitated by gradually adding NH_3 solution (25 wt%) until the pH value reached 10. The resultant solution was processed following the same steps as in the case of NiO.

The binary metal oxides (Mn_2O_3 + NiO) were prepared by the solid-state dispersion (SSD) method. Mn_2O_3 and NiO were thoroughly mixed in a 1 : 1 weight ratio using ethanol in an agate pestle and mortar; the solvent was then removed by evap-

oration during the mixing process. Samples prepared by this method were dried at 110 °C for 90 min and calcined at 450 °C for 6 h to obtain binary oxide catalysts. The resultant binary oxide was ground at a constant vibration rate of 300 rpm for 15 min in a Retsch MM 200 vibratory ball mill with 12 mm ZrO_2 milling balls in a ZrO_2 milling container.

Functionalisation with nitrogen and synthesis of catalysts

The synthesis of N-doped Mn_2O_3–NiO structures was achieved *via* the pyrolysis of a physical mixture of Mn_2O_3–NiO oxides and melamine (Sigma Aldrich). In this study, two different mass ratios of melamine to oxide (N : Mn_2O_3–NiO) were used: (1 : 1) and (1 : 2). The Mn_2O_3–NiO and melamine components were ground and mixed in a mortar to obtain a homogeneous mixture. A suitable crucible and tube furnace were used to put the powder mixture. Before the heat treatment, nitrogen gas was fed into the furnace environment at a certain flow rate, and this nitrogen atmosphere was maintained continuously throughout the process. In a nitrogen environment, the samples were heated to 400 °C for 2 h after the furnace had been preheated to that temperature. After the heating process was completed, the samples were cooled under a controlled nitrogen gas flow until the furnace temperature reached room temperature. Subsequently, the samples were extracted from the furnace and transferred to storage containers. The samples were labelled as N–Mn_2O_3–NiO (1 : 1) (S1), N–Mn_2O_3–NiO (1 : 2) (S1), N–Mn_2O_3–NiO (1 : 1) (S2), N–Mn_2O_3–NiO (1 : 2) (S2), N–Mn_2O_3–NiO (1 : 1) (S3), and N–Mn_2O_3–NiO (1 : 2) (S3).

Preparation of Pt/N–Mn_2O_3–NiO catalyst. A home microwave oven (Samsung, 800 W) was used to manufacture the Pt/N–Mn_2O_3–NiO catalysts with a microwave-assisted polyol approach. Using a magnetic stirrer, 100 mg of N–Mn_2O_3–NiO was dissolved in 50 mL of ethylene glycol (EG) in a beaker for 30 min to create a standard synthesis of Pt/N–N–Mn_2O_3–NiO catalysts with a Pt loading of 20 wt%. Following this, 2.6 mL of a 0.05 M H_2PtCl_6 salt solution was added, and the solution was mixed for 1 h using a magnetic stirrer. The resultant solution was exposed to 800 W of microwave heating for one minute. The solution was heated and then rapidly chilled in an ice bath. The oxide-supported Pt catalysts were then separated from the solvents by centrifuging the mixture at 7000 rpm. Ultimately, the mixture underwent filtration, was washed with acetone and deionised water, and then dried in an oven set at 100 °C for 12 h. The same procedure was used to synthesise all the samples.

Physical characterisation

An elemental analyser of the Leco CHNS-932 type was used to determine the quantity of nitrogen present in the oxide support materials. Surface area and pore size distributions of synthesised N–Mn_2O_3–NiO structures were examined with Micromeritics 3Flex Brunauer–Emmett–Teller (BET) Analyser. X-ray photoelectron spectroscopy (XPS) using the Specs-Flex XPS instrument, with an energy range of 200 eV to 4 keV, yielded valuable information about the materials' compositions, surface oxidation states, and electronic structure. The XPS analysis yielded both general and partial spectra of the materials. Additionally, the sub-peaks of the N1 partial spectra were obtained by using OriginPro 9.0. The amount of Pt in the N–Mn_2O_3–NiO catalysts was analysed using an Agilent 7800 ICP-MS inductively coupled plasma mass spectrometer. The crystal structure of nitrogen-doped support materials was determined using X-ray diffraction (XRD) with a PANalytical Empyrean instrument. The XRD analysis was performed using CuKα radiation with a wavelength of 1.5406 Å and a scan range of 10° to $2\theta \leq 90°$. The dispersion of micro/nanostructures and the crystal structure of metal on the support material were analysed using a Hitachi HighTech HT7700 transmission electron microscope (TEM). From the TEM pictures, a total of 100 nanoparticles were selected, and their sizes were manually determined using ImageJ software. The size distributions were analysed using the OriginPro 9.0 program, and histograms were obtained.

Electrochemical studies were conducted using cyclic voltammetry, linear scan voltammetry with a rotating disc electrode and electrochemical impedance spectroscopy (EIS). Experimental details of electrode preparation and electrochemical measurements are given in the SI.

Results and discussion

Catalyst physicochemical characterisation

The nitrogen doping of oxide structures was successfully achieved with an N amount in the 9.10–17.8 wt% range, as determined by elemental analysis (Table S1). Pt was subsequently loaded on the synthesised support materials by the microwave reduction method. The achieved Pt loadings on the support material closely match the nominal value of 20 wt% (Table S2).

Surface area and pore structure are defined as essential characteristics of catalyst support materials, and they have a significant impact on the catalyst's activity. Fig. S1 shows the N_2-adsorption/desorption isotherms and pore size distributions for the N-doped oxide structures. These structures display a Type IV isotherm according to IUPAC classification, indicating the presence of both mesopores and micropores. Capillary condensation occurs within mesopores, where gas molecules are adsorbed, leading to the formation of a hysteresis loop.[21] This hysteresis is observed in the relative pressure (P/P_0) range of 0.8–1.0, Fig. S1(a–c). However, in the case of N–Mn_2O_3–NiO (1 : 2) (S2) structure, hysteresis extends up to a relative pressure (P/P_0) of 0.4, resembling Type-3 hysteresis loops. This type of hysteresis loop shows the presence of sheet-like pores within the structure. Fig. S1 presents the pore size distribution curves, which reveal differences in textural properties as suggested by the N_2 isotherms. The inner graphs show variations in pore size distributions from 0 to 30 nm. The data indicate that most pores in the N–Mn_2O_3–NiO structures are between 0 and 5 nm wide. These structures, designed as catalyst support materials, exhibit mesoporous characteristics within this size range. Changes in pore size distribution

Table 1 BET analysis results of support materials

Sample	BET surface area ($m^2\ g^{-1}$)	BJH adsorption cumulative pore volume ($cm^3\ g^{-1}$)	BJH desorption cumulative pore volume ($cm^3\ g^{-1}$)	BJH adsorption average pore width (nm)	BJH desorption average pore width (nm)
N–Mn_2O_3–NiO (1 : 1) (S1)	20.31	0.226	0.227	40.86	38.33
N–Mn_2O_3–NiO (1 : 2) (S1)	28.13	0.241	0.241	30.56	29.04
N–Mn_2O_3–NiO (1 : 1) (S2)	24.62	0.087	0.087	12.33	11.44
N–Mn_2O_3–NiO (1 : 2) (S2)	37.71	0.118	0.119	10.94	9.79
N–Mn_2O_3–NiO (1 : 1) (S3)	2.77	0.012	0.012	16.18	15.45
N–Mn_2O_3–NiO (1 : 2) (S3)	3.05	0.020	0.019	21.41	20.82

also affect the BET surface area of the N-doped structures. Additionally, the effect of the nitrogen doping ratio (1 : 1 and 1 : 2) on the surface morphology of the composites was evaluated based on the BET surface area and pore structure properties determined by the BJH method (Table 1). The results reveal that the amount of nitrogen doping is a significant determinant of both the specific surface area and pore structure. Lower surface area values were obtained for a nitrogen doping level of 1 : 1. In samples S1 and S2, nitrogen doping with a 1 : 1 melamine-to-support ratio resulted in lower surface area values. In the S3 groups, significantly lower surface areas were achieved at both doping ratios. This suggests that synthesis under less basic conditions limits porosity formation, regardless of nitrogen content, and that pH plays a crucial role in determining the structure of the resulting material. Furthermore, if the nitrogen content exceeds a certain level, the porous structure may become partially blocked, micropores may convert into mesopores, or pore walls may collapse during doping, resulting in a lower surface area. This assessment is also supported by data on pore volume and average pore diameter. Therefore, not only nitrogen content but also the preservation of pore structure and the homogeneous distribution of nitrogen throughout the structure are critical for improving surface properties. All findings reveal that the combined evaluation of the melamine-to-support ratio and synthesis pH is the key factor in controlling the structural properties of the composites.[22]

To identify the crystalline phases in the synthesised structures, the samples were characterised by X-ray diffraction (Fig. 1). The peaks observed at ~32.9°, 38.2°, and 55.1° in all samples belong to the (222), (400), and (440) planes of the Mn_2O_3 structure. The sharp peaks at 37.2°, 43.2°, 62.8°, 75.2°, and 79.3° are attributed to the (111), (200), (220), (311), and (222) planes of NiO, respectively. Again, characteristic diffraction peaks were observed at 18.5°, 30.5°, and 57.2°, corresponding to the (111), (200), and (511) planes of $NiMn_2O_4$ in all catalyst structures. The characteristic peaks of Pt face cubic centred (fcc) at 40.1°, 46.5°, 68.0°, and 81.9° correspond to the (111), (200), (220), and (311) planes, respectively. Furthermore, an increase in the nitrogen content in the samples has resulted in a relative widening of the peaks.[16,23]

Fig. 2 presents the XPS survey spectra of the synthesised samples. Distinct peaks corresponding to C 1s, N 1s, O 1s, Mn 2p, and Ni 2p are observed at binding energies of 284.7 eV, 400.7 eV, 532.9 eV, 642.6 eV, and 855.0 eV, respectively. The

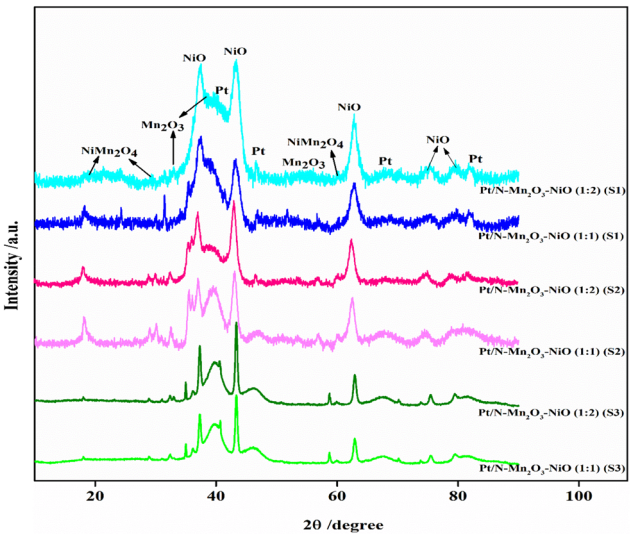

Fig. 1 XRD patterns of the synthesised catalysts.

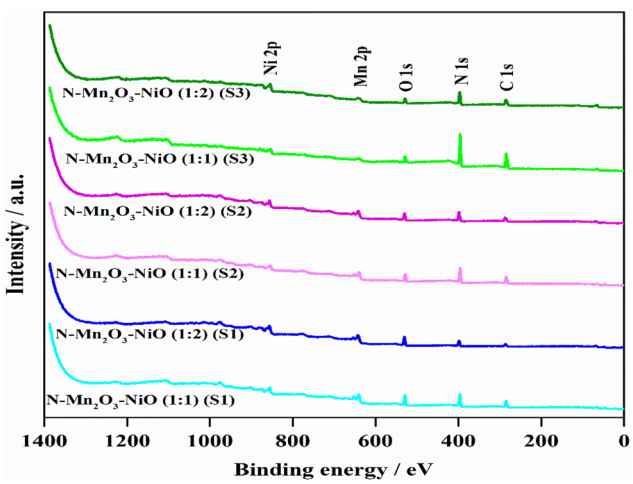

Fig. 2 XPS general spectrum of synthesised N–Mn_2O_3–NiO structures.

prominent signals for Mn, Ni, and O confirm the presence of the constituent elements of the support materials. Notably, the N 1s peak becomes increasingly sharp with higher nitrogen content, suggesting enhanced nitrogen incorporation. The C 1s peak is attributed to carbon atoms derived from melamine, which was used as the nitrogen source during synthesis.

The successful N-doping of the support material as targeted (Table S1), with a high intensity of the N 1s peak, enables the decomposition of the N 1s peak into various nitrogen species. The high-resolution XPS spectra of the nitrogen-doped support materials in the N 1s region are displayed in Fig. 3. When the samples' N 1s spectra were decomposed into their sub-peaks, pyridinic-N, pyrrolic-N, graphitic-N, and pyridinic N-oxide showed their peaks at binding energies of 398.07 ± 0.5 eV, 398.65 ± 0.5 eV, 399.25 ± 0.5 eV, and 400.10 ± 0.5 eV, respectively. It is well established that the electrochemical activity is linked more to these types of nitrogen species than to the overall nitrogen content.[24] Nitrogen in the pyridine structure contributes one or two π electrons to the aromatic π system and bonds with two nearby carbon atoms in six-sided or five-sided carbon rings. Graphite-type nitrogen lets three surrounding carbon atoms connect with a carbon atom entering the sp^2

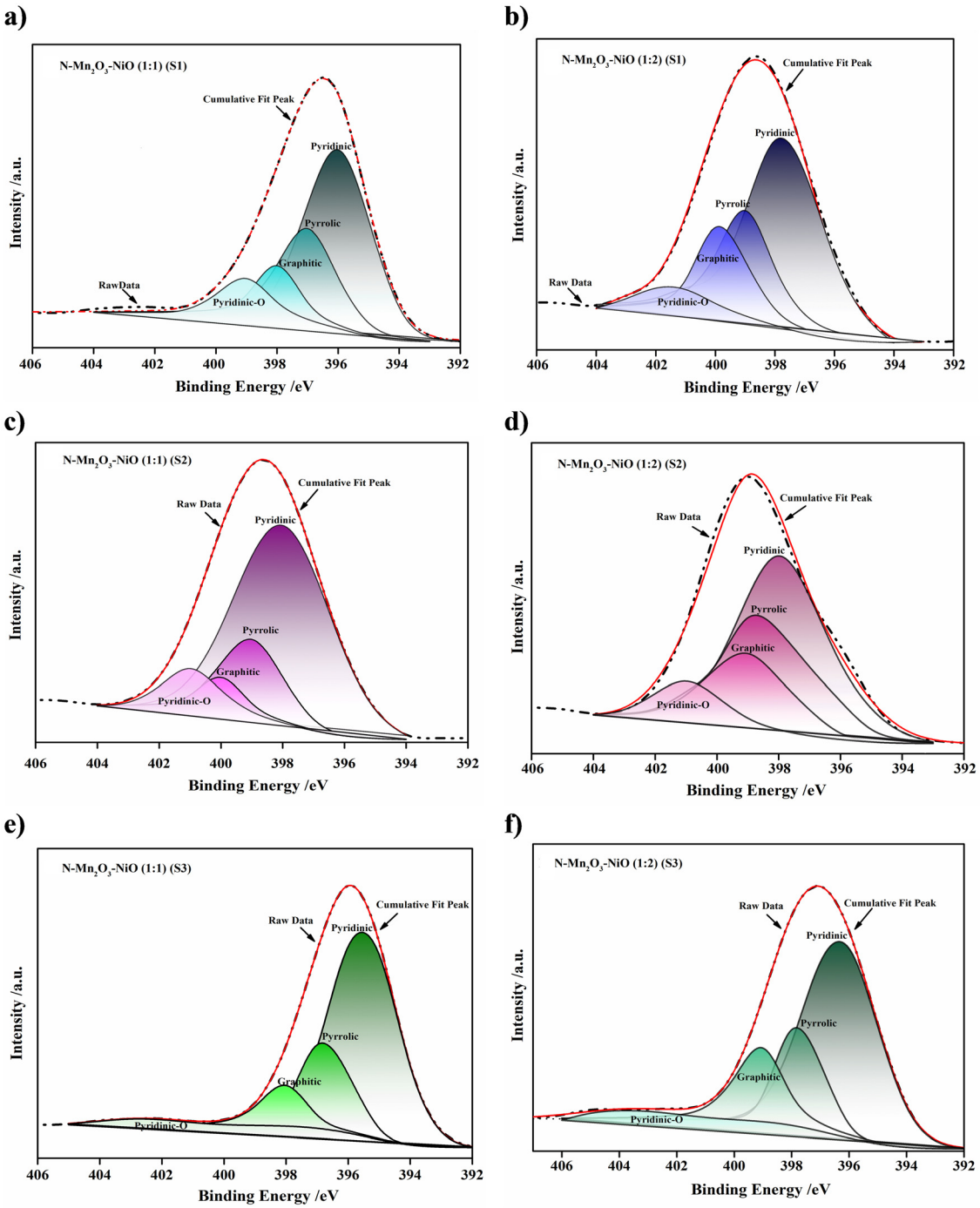

Fig. 3 N 1s high-resolution XPS spectra of (a) N–Mn_2O_3–NiO (1 : 1) (S1), (b) N–Mn_2O_3–NiO (1 : 2) (S2), (c) N–Mn_2O_3–NiO (1 : 1) (S2), (d) N–Mn_2O_3–NiO (1 : 2) (S2), (e) N–Mn_2O_3–NiO (1 : 1) (S3), (f) N–Mn_2O_3–NiO (1 : 2) (S3).

hybridisation state. Bonds developed by two carbon and one oxygen atom define the pyridinic N-oxide structure. Deconvolution analysis shows that the primary configurations in the synthesised metal oxide-based structures were pyrrolic-N and pyridinic-N.[25] The data for the nitrogen element obtained by XPS confirm the elemental analysis findings presented in Table S1. The peaks in the N 1s XPS spectra of the sample groups doped with a (1 : 1) ratio are significantly higher, and the peaks belonging to low-binding-energy pyridinic and pyrrolic nitrogen compounds are particularly high compared to other peaks. This indicates that nitrogen doping promotes the formation of more active nitrogen centres at edge and defect sites on the support material structures. In contrast, in samples with a (1 : 2) ratio, the intensity of the N 1s peaks decreased due to the decrease in total nitrogen content, resulting in a narrower area. The contribution of pyridinic and pyrrolic nitrogen species decreased, while the relative proportion of the graphitic nitrogen component increased. This finding suggests that the limited amount of nitrogen is primarily localised to more graphitic locations within the support material lattice and that active nitrogen formation at edge/defect sites is limited. While increasing the graphitic N ratio offers the potential to improve the material's electrical conductivity, it can negatively affect catalytic performance by limiting reactive centre formation due to the limited active surface area.[26] The percentages of different N-species were calculated by dividing the area of individual peaks in the N 1s spectrum by the total area of the four peaks (Table 2). N–Mn_2O_3–NiO (1 : 1) (S3) sample contains a higher proportion of pyridinic (66.46%) and pyrrolic (21.09%) nitrogen compared to the other samples. Nitrogen doping plays a critical role in electrocatalytic processes by regulating the electronic properties of materials and promoting the formation of active centres. Pyridinic and pyrrolic nitrogen configurations, in particular, constitute active centres for reactions such as HER, ORR, and OER, due to their capacity to alter charge distribution and electron density. Qu *et al.*[27] reported that high onset potentials and current densities are achieved in catalysts rich in pyridinic nitrogen, as these regions serve as suitable centres for the activation of the O_2 molecule. Similarly, Gong *et al.*[28] reported that the synergistic effect of pyridinic and graphitic nitrogen significantly increased catalytic efficiency by promoting the four-electron ORR pathway. It was also stated that the electron delocalisation provided by pyridinic nitrogen accelerated charge transfer and supported the stability of active sites. Zhang *et al.*[29] determined that N-doped carbon-supported Pt electrocatalysts with high pyrolic and pyridinic nitrogen contents and no other nitrogen species exhibited approximately three times higher ORR activity compared to Pt/XC electrocatalysts without nitrogen doping. A study by Ning *et al.*[30] reported that the sample with the highest pyridinic-N/graphitic-N ratio exhibited the highest ORR activity, a result consistent with the view that pyridinic nitrogen provides the most active sites for ORR. The obtained data suggest that samples with a 1 : 1 doping ratio offer greater advantages in terms of potential surface reactivity and catalytic activity due to their higher pyridinic/pyrrolic nitrogen content, whereas samples with a (1 : 2) doping ratio may exhibit more limited performance in this regard due to their lower active nitrogen content.

TEM and HR-TEM analysis were employed to examine the structure and size of the particles in the Pt/N–Mn_2O_3–NiO catalysts in greater detail (Fig. 4). Some aggregation of nanoparticles on the support material was observed, possibly due to the insufficient mixing of the metal precursor and the support material. Additionally, the surface area of the support material is another parameter that affects the homogeneous distribution of Pt particles. In this direction, it can be seen that agglomeration is more pronounced in the S3 structured support material, which has a lower surface area. The TEM images of the catalysts reveal that the particles are nearly spherical. The mean particle size values derived from the TEM analysis images were calculated using ImageJ software, yielding average sizes within a narrow range of 3 to 4 nm. Specifically, Pt particles were of *ca.* 3.61 nm, 3.73 nm, 3.43 nm, 3.21 nm, 4.02 nm, and 3.82 nm size for the Pt/N–Mn_2O_3–NiO (1 : 1) (S1), Pt/N–Mn_2O_3–NiO (1 : 2) (S1), Pt/N–Mn_2O_3–NiO (1 : 1) (S2), Pt/N–Mn_2O_3–NiO (1 : 2) (S2), Pt/N–Mn_2O_3–NiO (1 : 1) (S3), and Pt/N–Mn_2O_3–NiO (1 : 2) (S3) catalysts, respectively. However, despite Pt particle size remaining constant over different synthesis methods, factors such as the chemical composition and electronic characteristics of the BMO support, Pt–BMO interface interactions, and nitrogen doping directly affect the surface electronic properties and charge density of Pt nanoparticles, thus playing a decisive role in electrochemical activity.

Table 2 Chemical bonding states of N 1s spectra of support materials

Sample	Pyridinic-N (%)	Pyrrolic-N (%)	Graphitic-N (%)	Pyridinic N-oxide (%)
N–Mn_2O_3–NiO (1 : 1) (S1)	54.22	26.99	10.47	8.298
N–Mn_2O_3–NiO (1 : 2) (S1)	51.54	22.86	20.54	5.045
N–Mn_2O_3–NiO (1 : 1) (S2)	55.42	13.78	18.52	12.26
N–Mn_2O_3–NiO (1 : 2) (S2)	43.10	22.51	23.41	10.95
N–Mn_2O_3–NiO (1 : 1) (S3)	66.46	21.09	10.12	2.316
N–Mn_2O_3–NiO (1 : 2) (S3)	58.75	19.77	17.97	3.483

Double-layer capacitance investigation

To quantify the electric double-layer capacitance (C_{dl}) and calculate the ECSA, cyclic voltammograms were obtained at different scan rates in 0.1 M KOH using a short potential window centred around the open-circuit potential of each catalyst. Subsequently, a plot of $\Delta j/2 = f(\nu)$ was drawn, where Δj is the difference between the anodic and cathodic current density, j_a–j_c (mA cm^{-2}), measured approximately at the midpoint of the CV curve (around 1 V *vs.* RHE), and ν (mV s^{-1}) is

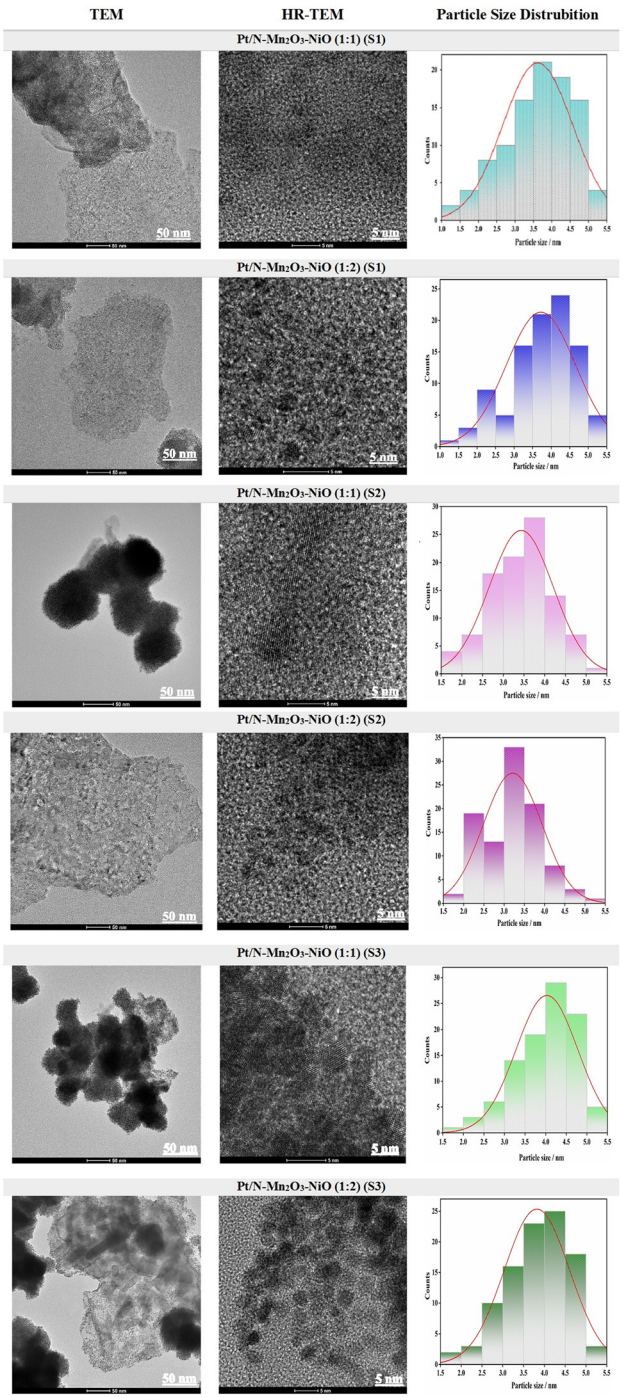

Fig. 4 TEM (50 nm scale bar) and HR-TEM (5 nm scale bar) images of catalysts and Pt particle size distributions (left to right: TEM – HRTEM – Pt particle size histograms).

the rate of polarisation of the working electrode. The C_{dl} was then determined as the slope of the $\Delta j/2 = f(\nu)$ graph for each catalyst. A reference value of 40 μF cm^{-2} per 1 cm^2 of surface area was used for estimating the ECSA from C_{dl}, as this is the most common value for the KOH solution found in the literature.[31] Initially, cyclic voltammograms of binary oxide Mn_2O_3–NiO doped with nitrogen (with two different ratios of Mn_2O_3–NiO to nitrogen, 1 : 1 and 1 : 2) were recorded, followed by voltammograms of the same oxides decorated with Pt (Fig. S2). The highest C_{dl} of 0.64 mF cm^{-2} was obtained in the case of Pt/N–Mn_2O_3–NiO (1 : 1) (S1), corresponding to the highest ECSA of 16.0 cm^2 per 1 cm^2 of geometric surface area. Lower C_{dl} values corresponding to ECSAs of 6.25 cm^2 and 6.00 cm^2 were obtained for N–Mn_2O_3–NiO (1 : 1) (S1) and N–Mn_2O_3–NiO (1 : 2) (S1), respectively. The C_{dl} value for Pt/N–Mn_2O_3–NiO (1 : 2) (S1) was found to be 0.22 mF cm^{-2}, which corresponds to an ECSA of 5.50 cm^2.

The recorded cyclic voltammograms of the second set of synthesised catalysts are shown in Fig. S3. The highest C_{dl} value was obtained for Pt/N–Mn_2O_3–NiO (1 : 1) (S2) (2.53 mF cm^{-2}), corresponding to an ECSA of 63.3 cm^2. In contrast, the calculated ECSA values for N–Mn_2O_3–NiO (1 : 1) (S2), N–Mn_2O_3–NiO (1 : 2) (S2), and Pt/N–Mn_2O_3–NiO (1 : 2) (S2) were significantly lower, amounting to only 12.3 cm^2, 6.25 cm^2, and 20.3 cm^2, respectively.

The recorded cyclic voltammograms of the third set of synthesised catalysts are shown in Fig. S4. As in the case of the previous two syntheses, the highest value of C_{dl}, 2.38 mF cm^{-2}, was obtained for Pt/N–Mn_2O_3–NiO (1 : 1) (S3), corresponding to an ECSA of 59.5 cm^2. A slightly lower ECSA value of 46.3 cm^2 was calculated Pt/N–Mn_2O_3–NiO (1 : 2) (S3). The pure N-doped binary oxides, N–Mn_2O_3–NiO (1 : 1) (S3) and N–Mn_2O_3–NiO (1 : 2) (S3) showed similar ECSA values of 8.25 cm^2 and 8.75 cm^2 per 1 cm^2 of the geometric surface area of the electrode.

A comparison of all the obtained C_{dl} and ECSA values for the investigated catalysts is presented in Table S3. The Pt-decorated materials exhibited significantly higher ECSA values than the pure N-doped binary oxides. Moreover, Pt-decorated materials with an N to Mn_2O_3–NiO ratio of 1 : 1 were characterised by a higher ECSA compared to those with an N to Mn_2O_3–NiO ratio of 1 : 2.

The incorporation of Pt into N-doped transition metal oxides has been shown to significantly enhance capacitive currents, primarily due to synergistic improvements in electronic conductivity, surface characteristics, and interfacial charge dynamics.[32] Pt facilitates rapid electron transport within the electrode, effectively reducing internal resistance and enabling more efficient charging and discharging of the electric double layer. Additionally, the incorporation of Pt nanoparticles can increase the ECSA by introducing surface roughness and porosity, thereby providing more sites for double-layer formation.[33] At the interface, strong electronic interactions between Pt and the N-doped TMO matrix can lead to beneficial charge redistribution, further increasing C_{dl}. Moreover, Pt promotes faster ion adsorption and desorption kinetics (especially in acidic electrolytes), which supports the rapid accumulation of surface charges characteristic of capacitive behaviour.[34] Finally, Pt can improve charge separation and suppress recombination processes in systems where pseudocapacitive contributions are present, further boosting the observed current response. The synergy between Pt addition and nitrogen doping thus led to a

pronounced increase in capacitive currents for the decorated TMO materials.[35]

Although TEM analysis revealed relatively similar Pt nanoparticle sizes across the S1, S2, and S3 samples, the observed differences in ECSA augmentation (2.56× for S1 (1 : 1), 5.16× for S2 (1 : 1), and 7.12× for S3 (1 : 1) compared to their non-Pt decorated analogues) suggest that additional factors beyond apparent particle size influence the electrochemical behaviour. Notably, intrinsic differences in the physicochemical properties of the deposited Pt, including crystallinity, surface energy, and electronic structure, may vary subtly between samples depending on the synthesis environment and precursor–substrate interactions, thereby affecting the density of active sites.[36] Moreover, variations in the synthesis protocols of the N-doped TMO substrates themselves may have impacted Pt anchoring, dispersion stability, and interfacial charge transfer. Post-synthesis factors such as catalyst ink formulation, degree of dispersion, and electrode fabrication also play a critical role. Poor ink dispersion during film preparation may have led to localised Pt clustering and uneven ionomer distribution, reducing surface accessibility and limiting double-layer formation, while improved ink homogeneity and film morphology may have facilitated more uniform Pt distribution and higher surface utilisation.[37] These findings emphasise that both the synthesis of the material and the post-synthesis handling, particularly ink formulation and deposition, are key to optimising the electrochemical performance of Pt-modified N-doped TMO materials.

Catalysis of the oxygen reduction reaction

ORR activity was assessed for each catalyst by first obtaining cyclic voltammograms at 0 rpm in nitrogen- and oxygen-saturated 0.1 M KOH, followed by linear sweep voltammetry (LSV) at varying rotation speeds. The experimental results for the material produced *via* the first synthesis are presented in Fig. S5 and S6. The Pt-decorated material, Pt/N–Mn_2O_3–NiO (1 : 1) (S1), showed a clear oxygen reduction maximum at 0.86 V (Fig. S5), a significantly higher diffusion-limited current values of −4.86 mA cm^{-2} at 1800 rpm and a half-wave potential, $E_{1/2}$, of 0.86 V compared to the other materials of this set (Fig. S6, Fig. 5). In the case of Pt/N–Mn_2O_3–NiO (1 : 2) (S1), the reduction maximum is observed at about 0.64 V. A lower value of j_d of −1.64 mA cm^{-2} and the half-wave potential of 0.64 V were obtained. As expected, pure N–Mn_2O_3–NiO (S1) oxides delivered lower performance (Table 3) with lower diffusion-limiting current densities of −2.66 and −1.89 mA cm^{-2} at 1800 rpm for N–Mn_2O_3–NiO (1 : 1) (S1) and N–Mn_2O_3–NiO (1 : 2) (S1), respectively. In the studied composites comprising Pt and N-doped Mn and Ni oxides, the primary catalytic sites for the ORR are considered to be Pt nanoparticles along with nitrogen species. Doping of BMO support with nitrogen alters the electronic structure of Pt by inducing electron transfer from the Pt nanoparticles to the nitrogen-doped support due to the higher electron affinity of N. This leads to a higher oxidation state of Pt and a shift in its d-band centre. The electron withdrawal

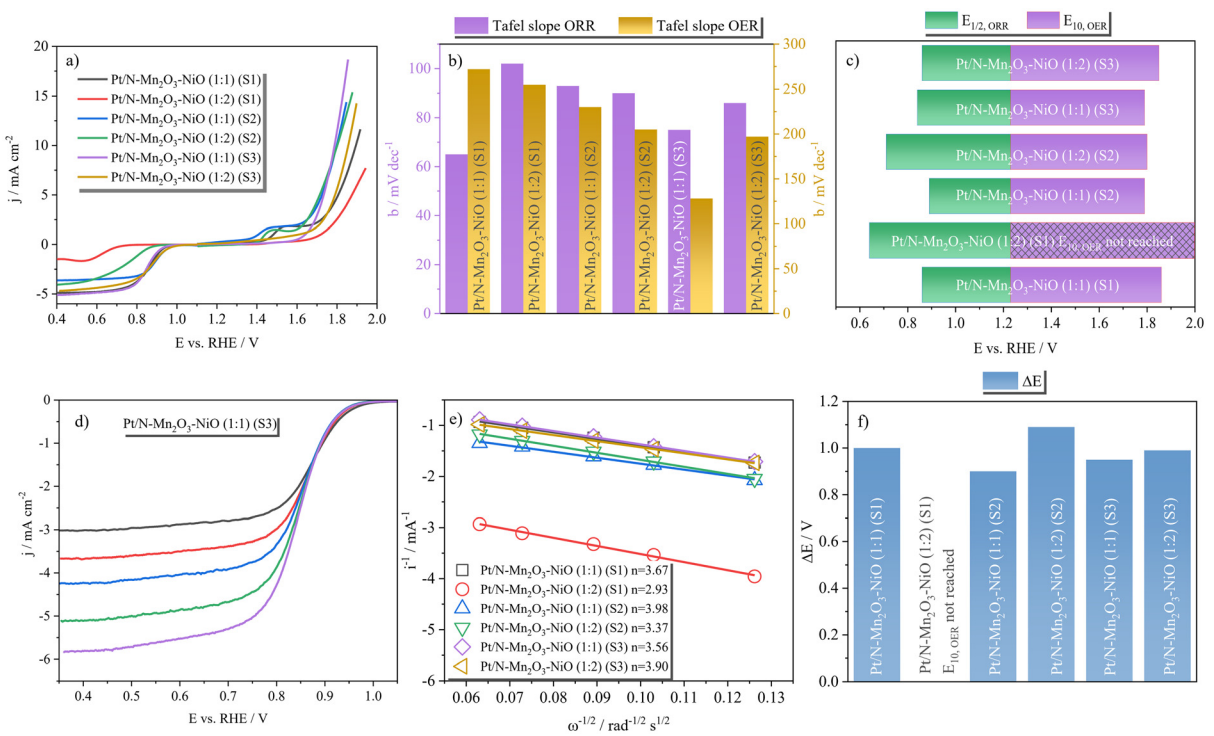

Fig. 5 (a) LSVs at 1800 rpm in ORR potential region and at 1200 rpm in OER potential region, (b) comparison of ORR and OER Tafel slopes, (c) comparison of $E_{1/2,\ ORR}$ and $E_{10,\ OER}$, (d) LSVs at different rotation rates for the best performing Pt/N–Mn_2O_3–NiO (1 : 1) (S3), (e) Koutecký–Levich plots, and (f) comparison of ΔE values for all Pt-decorated catalysts.

further weakens the interaction between Pt and adsorbed ORR intermediates, preventing the catalyst poisoning and facilitating efficient oxygen reduction. Mn_2O_3 can provide extra active sites *via* the formation of Mn^{3+}/Mn^{2+} redox couples that participate in ORR. Mn_2O_3 further facilitates hydrogen peroxide decomposition, thus favouring a four-electron ORR mechanism. As mentioned, XPS analysis revealed the presence of different N species that contribute to the increase in the number of active sites: pyridinic-N, pyrrolic-N, graphitic-N, and pyridinic-N-oxide, with pyrrolic-N and pyridinic-N being predominant (Table 2). Pyridinic-N typically decreases the onset potential for the ORR, and graphitic-N functions as a central active site for ORR, enabling the attainment of a diffusion-limited current density. On the other hand, pyrrolic-N has little impact on the ORR activity of nitrogen-doped materials.[31]

The LSV curves at 1800 rpm were subjected to Tafel analysis (Fig. S7(a)). The lowest Tafel slope (b) value was obtained for Pt/N–Mn_2O_3–NiO (1 : 1) (S1) (65 mV dec^{-1}), indicating faster ORR kinetics for this material compared to the other three materials obtained by this synthesis method. For N–Mn_2O_3–NiO (1 : 1) (S1), N–Mn_2O_3–NiO (1 : 2) (S1), and Pt/N–Mn_2O_3–NiO (1 : 2) (S1), the calculated b values amount to 96 mV dec^{-1}, 115 mV dec^{-1}, and 102 mV dec^{-1}, respectively.

To determine the number of exchanged electrons (n) during an electrochemical reaction, Koutecký–Levich (K–L) analysis is performed, an electrochemical method used to separate the kinetic current density (j_k) from the diffusion-limited current density (j_d) in rotating disc electrode experiments. The number of exchanged electrons, n, during the elementary step of the reaction is determined using the K–L equation (eqn (1)),

$$\frac{1}{j} = \frac{1}{j_k} + \frac{1}{j_D} = \frac{1}{j_k} + \frac{1}{B + \omega^{1/2}} \quad (1)$$

where j is the measured current density, ω is the rotation rate (rad s^{-1}), and B is the Levich constant, related to diffusion and solution properties. Thus, the slope of $j^{-1} = f(\omega^{-1/2})$ allows determination of n through the Levich equation (eqn (2)),

$$B = 0.62nFAD^{2/3}\nu^{-1/6}C \quad (2)$$

where F is Faraday's constant, D is the diffusion coefficient of the reactant (oxygen), A is the electrode surface area, ν is the kinematic viscosity of the electrolyte solution, and C is the bulk concentration of the reactant (oxygen). Fig. S7(b) displays K–L plots constructed based on linear sweep voltammetry data obtained at different rotation speeds, and used for the calculation of the number of exchanged electrons during ORR. The calculated n value was 3.67 for Pt/N–Mn_2O_3–NiO (1 : 1) (S1) and 2.93 for Pt/N–Mn_2O_3–NiO (1 : 2) (S1), indicating that ORR proceeds *via* mixed $2e^-$ and $4e^-$ mechanisms, with the $4e^-$-mechanism being predominant in the case of the former. For nitrogen-doped oxides, the value of n was calculated to be 3.04 and 2.04 for N–Mn_2O_3–NiO (1 : 1) (S1) and N–Mn_2O_3–NiO (1 : 2) (S1), respectively.

Upon comparison of all analysed ORR parameters, Pt/N–Mn_2O_3–NiO (1 : 1) (S1) emerged as the most effective catalyst synthesised using this method, achieving the highest diffusion-limited current density and half-wave potential, the lowest Tafel slope, and the highest number of transferred electrons.

Following the analysis of the first set of materials, the same procedure (cyclic voltammetry and LSVs at varying scan rates) was applied to the second set of materials, as shown in Fig. S8 and S9. The oxygen reduction maximum is observed at the cyclic voltammograms in 0.1 M KOH saturated with O_2 at 0.91 V and 0.80 V for Pt/N–Mn_2O_3–NiO (1 : 1) (S2) and Pt/N–Mn_2O_3–NiO (1 : 2) (S2), respectively. Higher j_d were delivered by the Pt/N–Mn_2O_3–NiO (1 : 2) (S2) catalyst (−3.90 mA cm^{-2}) and Pt/N–Mn_2O_3–NiO (1 : 1) (S2) (−3.60 mA cm^{-2}) compared to the undecorated oxides. N–Mn_2O_3–NiO (1 : 1) (S2), and N–Mn_2O_3–NiO (1 : 2) (S2) delivered j_d values of −3.17 mA cm^{-2} and −2.76 mA cm^{-2}, respectively. The values of the half-wave potential were determined to be 0.67 V, 0.70 V, 0.89 V, and 0.71 V for N–Mn_2O_3–NiO (1 : 1) (S2), N–Mn_2O_3–NiO (1 : 2) (S2), Pt/N–Mn_2O_3–NiO (1 : 1) (S2), and Pt/N–Mn_2O_3–NiO (1 : 2) (S2), respectively.

Tafel slopes (Fig. S10(a)) were of similar values for Pt-decorated and non-decorated N-doped materials within a 82–93 mV dec^{-1} range (Table 3).

The Koutecký–Levich analysis (Fig. S10(b)) revealed that oxygen reduction on Pt/N–Mn_2O_3–NiO (1 : 1) (S2) proceeds mainly *via* the four-electron reduction mechanism, while on Pt/N–Mn_2O_3–NiO (1 : 2) (S2) and non-decorated BMOs, ORR proceeds *via* mixed kinetics. Namely, the number of exchanged electrons was calculated to be 3.98 and 3.37 for Pt/N–Mn_2O_3–NiO (1 : 1) (S2) and Pt/N–Mn_2O_3–NiO (1 : 2) (S2), respectively. For N–Mn_2O_3–NiO (1 : 1) (S2) and N–Mn_2O_3–NiO (1 : 2) (S2), the n was found to be 3.15 and 3.07, respectively.

As in the case of the materials obtained in the previous synthesis, the Pt-decorated catalyst with the BMO to N ratio of 1 : 1 (Pt/N–Mn_2O_3–NiO (1 : 1) (S2)) showed the overall best performance for ORR in terms of the highest number of exchanged electrons in the elementary step of the reaction, the highest value of $E_{1/2}$ and the second highest obtained j_d.

Fig. S11(a–d) show the results of the CV experiments obtained with the third set of materials. Clear oxygen reduction maxima can be observed at 0.70 V, 0.67 V, 0.88 V, and 0.90 V for N–Mn_2O_3–NiO (1 : 1) (S3), N–Mn_2O_3–NiO (1 : 2) (S3), Pt/N–Mn_2O_3–NiO (1 : 1) (S3), and Pt/N–Mn_2O_3–NiO (1 : 2) (S3), respectively. As expected, the Pt-decorated materials showed higher diffusion-limited current densities and higher half-wave potentials compared to the undecorated N-doped materials. The highest j_d value was reached by Pt/N–Mn_2O_3–NiO (1 : 1) (S3) (−4.98 mA cm^{-2}), which also delivered the highest kinetic current density (−15.27 mA cm^{-2}). Pt/N–Mn_2O_3–NiO (1 : 2) (S3) reached j_d of −4.53 mA cm^{-2} and j_k of −4.56 mA cm^{-2}, while N–Mn_2O_3–NiO (1 : 1) (S3) and N–Mn_2O_3–NiO (1 : 2) (S3) show significantly lower values. The half-wave potentials for these materials were determined to be 0.70 V, 0.63 V, 0.84 V, and 0.86 V for N–Mn_2O_3–NiO (1 : 1) (S3), N–Mn_2O_3–NiO (1 : 2) (S3), Pt/N–Mn_2O_3–NiO (1 : 1) (S3), and Pt/N–Mn_2O_3–NiO (1 : 2) (S3), respectively. Within this set of

materials, Pt/N–Mn_2O_3–NiO (1 : 1) (S3) exhibited the lowest Tafel slope value of 75 mV dec^{-1}, while N–Mn_2O_3–NiO (1 : 1) (S3), N–Mn_2O_3–NiO (1 : 2) (S3) and Pt/N–Mn_2O_3–NiO (1 : 2) (S3) showed slightly higher values of 91 mV dec^{-1}, 93 mV dec^{-1}, and 86 mV dec^{-1}, respectively (Fig. S13(a)). The number of exchanged electrons was calculated to be between 2.54 and 3.90, Fig. S13(b). The highest value of n was calculated for Pt/N–Mn_2O_3–NiO (1 : 2) (S3) (n = 3.90), while the lowest value was calculated for N–Mn_2O_3–NiO (1 : 2) (S3) (n = 2.54). For N–Mn_2O_3–NiO (1 : 1) (S3) and Pt/N–Mn_2O_3–NiO (1 : 1) (S3), it was calculated that n = 3.21 and n = 3.56, respectively.

Comparing the obtained results, both Pt-decorated materials from the third set showed similar ORR performance. On both materials, ORR proceeds mainly *via* the four-electron mechanism, and the j_d values reached with these two were among the highest of all tested materials. Furthermore, $E_{1/2}$ values for Pt/N–Mn_2O_3–NiO (1 : 1) (S3) and Pt/N–Mn_2O_3–NiO (1 : 2) (S3) were almost identical, indicating that with this synthesis method, the BMO to N ratio has a lower or no impact on catalytic performance than with the previous two syntheses.

OER performance

To evaluate the OER activity of the synthesised electrocatalysts, LSV was performed in 0.1 M KOH at 1200 rpm in the OER polarisation region. The resulting curves were analysed using Tafel analysis; Tafel plots are presented as insets within the corresponding figures. Comparing the polarisation curves for the materials from the first synthesis (Fig. S14(a)), it can be seen that the Pt/N–Mn_2O_3–NiO (1 : 1) (S1) catalyst exhibited significantly better performance in catalysing the investigated reaction. For this catalyst, a reaction onset potential of 1.48 V was recorded, while the current density of 10 mA cm^{-2} was achieved at an overpotential (η_{10}) of 0.63 V. The calculated Tafel slope value for this catalyst was 272 mV dec^{-1}. In the case of N–Mn_2O_3–NiO (1 : 1) (S1), N–Mn_2O_3–NiO (1 : 2) (S1), and Pt/N–Mn_2O_3–NiO (1 : 2) (S1), the onset potentials have slightly higher values, at 1.84 V, 1.82 V, and 1.72 V, respectively. The value of 10 mA cm^{-2} was not reached with these three catalysts in the investigated potential range. The Tafel slope values for N–Mn_2O_3–NiO (1 : 1) (S1), N–Mn_2O_3–NiO (1 : 2) (S1), and Pt/N–Mn_2O_3–NiO (1 : 2) (S1) were 267 mV dec^{-1}, 246 mV dec^{-1}, and 255 mV dec^{-1}, respectively.

Fig. S14(b) shows the results of testing the second set of synthesised catalysts. Similar to the first synthesis, the catalyst Pt/N–Mn_2O_3–NiO (1 : 1) (S2) exhibited the lowest onset potential for the reaction, with oxygen evolution starting at 1.14 V. The current density of 10 mA cm^{-2} with this catalyst was reached at an η_{10} of 0.56 V. The same current density with N–Mn_2O_3–NiO (1 : 1) (S2) and Pt/N–Mn_2O_3–NiO (1 : 2) (S2) was achieved at an overpotential of 0.67 V and 0.57 V, respectively, while with N–Mn_2O_3–NiO (1 : 2) (S2), the current density of 10 mA cm^{-2} was not reached. The OER on Pt/N–Mn_2O_3–NiO (1 : 2) (S2) starts at 1.44 V, while on N–Mn_2O_3–NiO (1 : 1) (S2) and N–Mn_2O_3–NiO (1 : 2) (S2), it starts at notably higher potentials of 1.70 V and 1.76 V, respectively. The highest Tafel slope values of 230 and 225 mV dec^{-1} were obtained for Pt/N–Mn_2O_3–NiO (1 : 1) (S2) and N–Mn_2O_3–NiO (1 : 2) (S2), respectively, while for Pt/N–Mn_2O_3–NiO (1 : 2) (S2) a value of 205 mV dec^{-1} was obtained. A lower value of b was obtained only with N–Mn_2O_3–NiO (1 : 1) (S2) (177 mV dec^{-1}).

Finally, the catalytic performance of the catalysts synthesised in the third synthesis was examined, in Fig. S14(c). It

Table 3 Comparison of ORR and OER parameters of synthesised electrocatalysts with literature data

	ORR parameters					OER parameters			
Material	j_d/mA cm^{-2}	j_k/mA cm^{-2}	$E_{1/2}$/V	b/mV dec^{-1}	n	η_{10} mA cm^{-2}/V	b/mV dec^{-1}	ΔE/V	Source
N–Mn_2O_3–NiO (1 : 1) S1	−2.66	−1.25	0.66	96	3.04	—	267	—	This work
N–Mn_2O_3–NiO (1 : 2) S1	−1.89	−1.04	0.65	115	2.04	—	246	—	This work
Pt/N–Mn_2O_3–NiO (1 : 1) S1	−4.86	−8.05	0.86	65	3.67	0.63	272	1.00	This work
Pt/N–Mn_2O_3–NiO (1 : 2) S1	−1.64	−0.52	0.64	102	2.93	—	255	—	This work
N–Mn_2O_3–NiO (1 : 1) S2	−3.17	−1.88	0.67	93	3.15	0.67	177	1.23	This work
N–Mn_2O_3–NiO (1 : 2) S2	−2.76	−0.14	0.70	82	3.07	—	225	—	This work
Pt/N–Mn_2O_3–NiO (1 : 1) S2	−3.60	−1.72	0.89	93	3.98	0.56	230	0.90	This work
Pt/N–Mn_2O_3–NiO (1 : 2) S2	−3.90	−0.34	0.71	90	3.37	0.57	205	1.09	This work
N–Mn_2O_3–NiO (1 : 1) S3	−2.71	−1.18	0.70	91	3.21	—	195	—	This work
N–Mn_2O_3–NiO (1 : 2) S3	−2.93	−2.44	0.63	93	2.54	—	189	—	This work
Pt/N–Mn_2O_3–NiO (1 : 1) S3	−4.98	−15.3	0.84	75	3.56	0.56	128	0.95	This work
Pt/N–Mn_2O_3–NiO (1 : 2) S3	−4.53	−4.56	0.86	86	3.90	0.62	197	0.99	This work
NiO/$NiCo_2O_4$	—	—	0.37	85.4	—	—	130	—	41
MnO/Co/PGC	—	—	0.78	69	—	—	77	—	42
MnO_2–$C_{(ultrathin\ amorphous)}$	−5.81	—	0.81	—	4.00	—	—	—	43
MnO_x/CNTs	−4.90	—	0.77	—	3.60	—	—	—	44
Pt/Mn_2O_3–NiO	−4.48	−4.34	0.79	62 and 109	3.73	0.54	154	0.98	15
PtNi/Mn_2O_3–NiO	−4.32	−3.10	0.79	63 and 103	3.99	0.53	140	0.97	15
Mn_2O_3–NiO	−1.93	−0.67	0.66	151	2.90	0.57	155	1.14	16
Mn_2O_3–NiO–N (1 : 1)	−2.75	−1.65	0.75	82	2.73	—	230	—	16
Pt/Mn_2O_3–NiO–N (1 : 1)	−4.69	−2.97	0.87	90	3.88	0.63	249	0.99	16
IrO_2	—	—	—	—	—	0.36	84	—	45
RuO_2	—	—	—	—	—	0.40	—	—	46
Pt/C (40 wt%)	−6.44	14.9	0.86	79 and 60	3.97	0.58	198	0.95	15

can be seen that the reaction starts the earliest on the Pt/N–Mn_2O_3–NiO (1 : 2) (S3) catalyst (onset potential of 1.61 V), followed by Pt/N–Mn_2O_3–NiO (1 : 1) (S3) (1.64 V). Higher onset potentials of 1.84 V and 1.73 V were observed for N–Mn_2O_3–NiO (1 : 1) (S3) and N–Mn_2O_3–NiO (1 : 2) (S3), respectively. Pt/N–Mn_2O_3–NiO (1 : 1) (S3) reaches 10 mA cm^{-2} current density earliest (minimum overpotential value of 0.56 V), while Pt/N–Mn_2O_3–NiO (1 : 2) (S3) reaches 10 mA cm^{-2} at an overpotential of 0.62 V. The current density of 10 mA cm^{-2} was not reached with the remaining two catalysts. As in the previous two sets investigations, the lowest Tafel slope value of 128 mV dec^{-1} was obtained for Pt/N–Mn_2O_3–NiO (1 : 1) (S3), while values of 195 mV dec^{-1}, 189 mV dec^{-1}, and 197 mV dec^{-1} were obtained for N–Mn_2O_3–NiO (1 : 1) (S3), N–Mn_2O_3–NiO (1 : 2) (S3), and Pt/N–Mn_2O_3–NiO (1 : 2) (S3), respectively.

EIS is typically used to gain a better insight into the origin of resistance in an electrochemical system. Nyquist and Bode plots of catalysts from all three syntheses in 0.1 M KOH at 1.8 V are shown in Fig. 6. All EIS data were fitted using the equivalent circuit shown in Fig. 6(a), and the comparison of EIS fit parameters is shown in Table S4. Notably, the solution and wiring resistance (R_s) values vary only slightly, from 46 Ω to 76 Ω, indicating the good experimental setup and the consistency of the performed experiments. On the other hand, charge-transfer resistance (R_{ct}) values range from 47.27 Ω for Pt/N–Mn_2O_3–NiO (1 : 1) (S3) to 605.9 Ω for N–Mn_2O_3–NiO (1 : 2) (S1), supporting the better performance of the Pt-decorated materials compared to the non-decorated BMOs. The two best-performing electrocatalysts, Pt/N–Mn_2O_3–NiO (1 : 1) (S3) and Pt/N–Mn_2O_3–NiO (1 : 1) (S2), showed the smallest values of R_{ct}, 47.27 Ω and 64.43 Ω, respectively. Nyquist plots of all investigated materials showed slight flattening of the semicircles, indicating dispersive capacitance,[38] which led to using the CPE (constant phase element) for fitting the data instead of the ideal capacitance. CPE is an empirical element that accounts for the capacitive element's non-ideal behaviour due to the surface's inhomogeneities. The effective capacitance C can be obtained from CPE using eqn (3),[39,40]

$$C = \text{CPE-T}^{1/\text{CPE-P}} R^{(1-\text{CPE-P})/\text{CPE-P}} \quad (3)$$

where R represents R_{ct}, CPE-T is the parameter obtained by fitting the EIS results, and CPE-P parameter can acquire values from 0 to 1, with CPE-P = 1 corresponding to the ideal capacitor. Investigated materials showed CPE-P values of 0.35 up to 0.74 with the two best-performing catalysts, Pt/N–Mn_2O_3–NiO (1 : 1) (S3) and Pt/N–Mn_2O_3–NiO (1 : 1) S2, showing the CPE-P of 0.67 and 0.65, respectively. The Bode plots for all tested materials exhibit a single time constant and a corresponding phase angle maximum in the mid-frequency range, consistent with a single semicircle observed in their Nyquist plots. This behaviour, reflected as a single semicircle in the Nyquist plots, is interpreted as the capacitive response of the double layer formed at the electrode/solution interface.

Results comparison and bifunctional performance assessment

The synthesised materials exhibited catalytic activity towards both oxygen reduction and oxygen evolution reactions, as demonstrated by testing in their respective potential regions. Furthermore, nitrogen content relative to the binary metal oxide (BMO) significantly affected catalytic activity. In the first two syntheses, increased nitrogen content led to enhanced ORR performance, with a 1 : 1 N–BMO ratio yielding superior diffusion-limited current densities and electron transfer numbers compared to an N–BMO with a 1 : 2 ratio. While the third synthesis showed a diminished nitrogen influence on diffusion-limited current density, the 1 : 1 N–BMO catalyst still exhibited a notably higher electron transfer number (3.21 for N–Mn_2O_3–NiO (1 : 1) (S3) *vs.* 2.54 for N–Mn_2O_3–NiO (1 : 2) (S3)), indicating nitrogen's continued role in improving activity and altering reaction kinetics. The impact of the N–BMO ratio persisted in Pt-decorated catalysts. Consistent with previous findings, the N–BMO 1 : 1 ratio in the first synthesis resulted in superior diffusion-limited current density and electron-transfer number compared to N–BMO 1 : 2. Conversely, the second synthesis showed a slight increase in diffusion-limited current density for the N–BMO 1 : 2 ratio, while the third synthesis reinforced the trend of higher nitrogen content correlating with enhanced diffusion-limited current. Contrary to the trend observed with diffusion-limited current density, the number of transferred electrons showed an inverse relationship in syntheses two and three for Pt-decorated materials. For instance, in the third synthesis, Pt/N–Mn_2O_3–NiO (1 : 1) (S3) demonstrated a lower electron-transfer number despite having a higher diffusion-limited current density compared to Pt/N–Mn_2O_3–NiO (1 : 2) (S3).

Of pure bimetallic oxides tested for the OER, only N–Mn_2O_3–NiO (1 : 1) (S2) reached a current density of 10 mA cm^{-2}, suggesting limited activity of pure oxides toward this reaction. In contrast, Pt-decorated catalysts, particularly Pt/N–Mn_2O_3–NiO (1 : 1) (S3) and Pt/N–Mn_2O_3–NiO (1 : 1) (S2), showed excellent performance, all achieving a benchmark current density of 10 mA cm^{-2} with the latter two requiring an overpotential of 0.56 V. Similar to the ORR results, higher nitrogen doping consistently enhanced catalytic performance for oxygen evolution. This suggests that the nitrogen content remains one of the key factors, enhancing the ECSA and overall material activity, regardless of minor adjustments to the synthesis process.

Investigation of the bifunctional performance of the materials provided better insight into the catalyst's ability to alternate between the two mentioned operating modes in the unitised regenerative fuel cells. As a measurement of the bifunctional performance, ΔE was used, representing the difference between the potential at which the material achieves a benchmark current density of 10 mA cm^{-2}, E_{10}, in the OER potential region and half-wave potential, $E_{1/2}$, in the ORR potential region. As can be seen from Fig. S14 and Fig. 5, not all materials reached 10 mA cm^{-2} within the investigated OER potential window, and therefore the determination of the ΔE parameter was not possible for these materials.

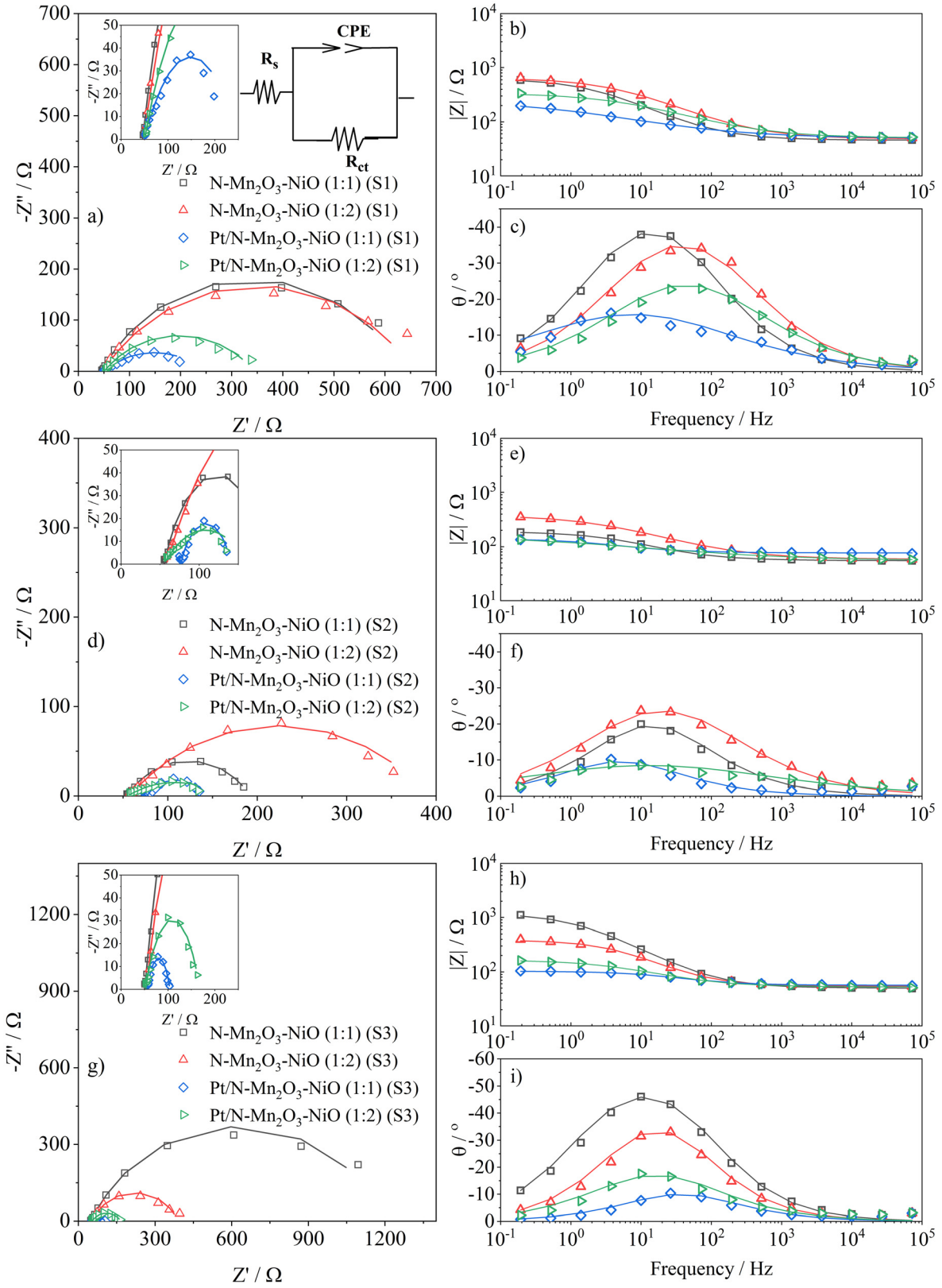

Fig. 6 Nyquist and Bode plots recorded at 1.8 V for materials from all three syntheses.

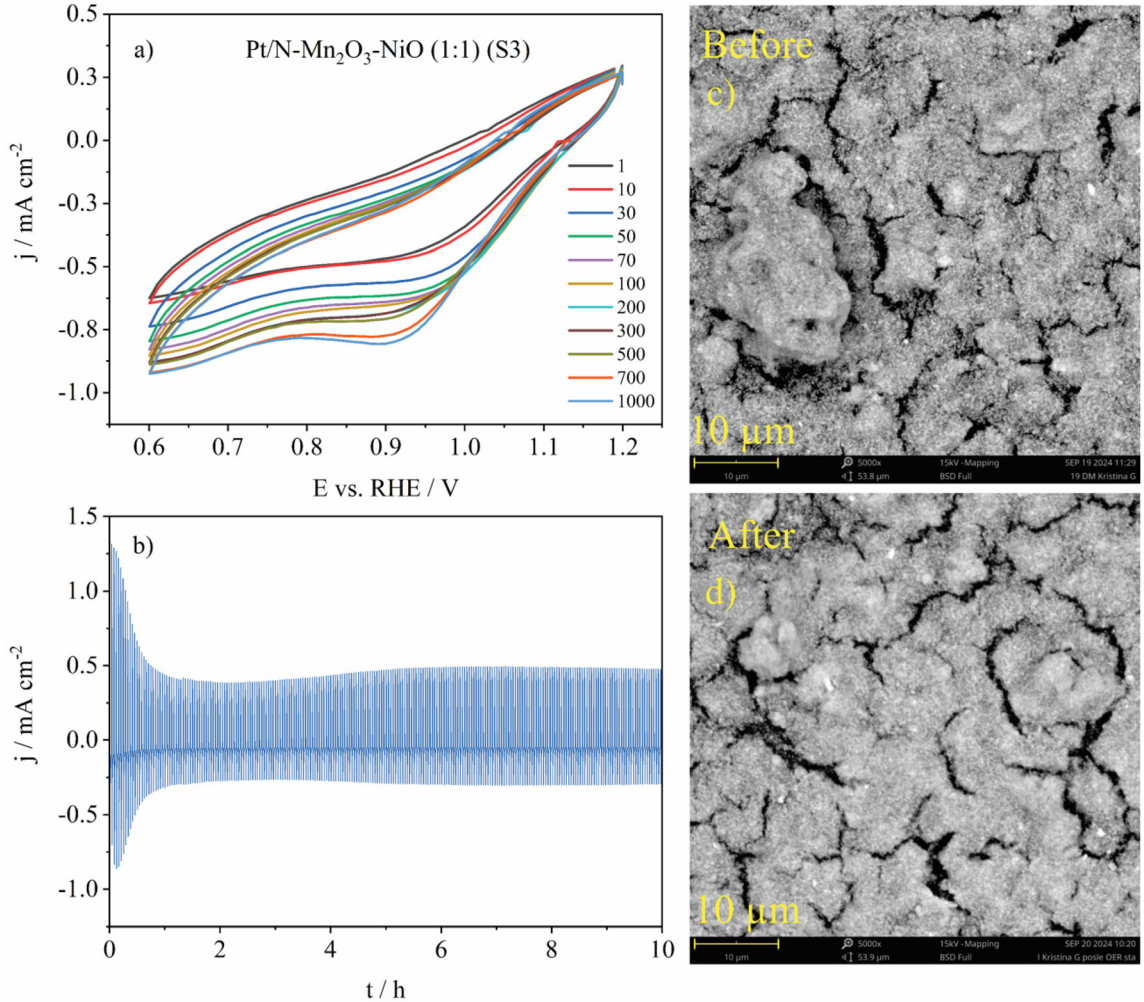

Fig. 7 Results of the (a) accelerated stress test (AST), (b) switch test, and SEM images (c) before and (d) after the AST of the best performing material, Pt/N–Mn_2O_3–NiO (1 : 1) (S3).

The determined ΔE values are presented in Table 3 and in Fig. 5(f). The smallest ΔE was calculated for the Pt/N–Mn_2O_3–NiO (1 : 1) (S2) of 0.90 V, indicating the best bifunctional performance. A somewhat higher value of this parameter was calculated for Pt/N–Mn_2O_3–NiO (1 : 1) (S3), 0.95 V. Both of these values are comparable with the values that were calculated for the commercial 40 wt% Pt/C catalyst in the authors' previous work (ΔE = 0.94 V), even though herein synthesised materials contained only 20 wt% of Pt.[15] The values were further comparable to that of undoped PtNi/Mn_2O_3–NiO (0.97 V) tested in the same work.[15] However, it should be kept in mind that when evaluating the bifunctional performance, all relevant parameters for both investigated reactions should be taken into account. For example, although Pt/N–Mn_2O_3–NiO (1 : 1) (S2) showed the smallest value of ΔE, Pt/N–Mn_2O_3–NiO (1 : 1) (S3) showed a significantly higher value of ORR j_d, −4.98 mA cm^{-2} compared with −3.60 mA cm^{-2} for Pt/N–Mn_2O_3–NiO (1 : 1) (S2), and both materials have achieved 10 mA cm^{-2} in OER mode at the same overpotential of 0.56 V. As authors suggested in their previous work,[10] the $E_{1/2}$ values and, consequently, calculated ΔE values should be taken with some reserve. Therefore, it might be better to use a potential at which a defined value of current density is achieved (*e.g.*, 3 mA cm^{-3}) instead of the $E_{1/2}$ for the determination of ΔE.

For the rest of the synthesised materials, significantly higher ΔE values were calculated, ranging from 0.99 V in the case of Pt/N–Mn_2O_3–NiO (1 : 2) (S3) up to 1.23 V for N–Mn_2O_3–NiO (1 : 1) (S2). It should also be mentioned that N–Mn_2O_3–NiO (1 : 1) (S2) is the only Pt-undecorated material that achieved 10 mA cm^{-2} in OER mode and the only Pt-undecorated material for which we were able to determine ΔE.

Study of electrocatalysts' stability

The stability of the best-performing bifunctional catalyst, Pt/N–Mn_2O_3–NiO (1 : 1) (S3), was first investigated using the accelerated stress test (AST) method in the ORR potential region. A slight increase in the current over time was recorded during continuous cycling (Fig. 7(a)), likely due to the activation of

the electrode surface. SEM images of the electrode before and after the AST experiments reveal an almost identical morphology, indicating the remarkable stability of the material during prolonged cycling (Fig. 7(c and d)). SEM images at different magnifications, as well as the EDS mapping of the electrode before and after the AST, are shown in Fig. S15.

The results of the switch test performed with the Pt/N–Mn_2O_3–NiO (1 : 1) (S3) are presented in Fig. 7(b). This test simulates real-life conditions in which a bifunctional material operates under constant switching between reduction and oxidation potentials. The switch test also demonstrated the remarkable stability of the synthesised material, where the ORR and OER currents, after an initial drop, remained almost unchanged during the ten-hour experiment.

This study demonstrated the successful development of Pt/N–Mn_2O_3–NiO (1 : 1) (S3) bifunctional ORR/OER electrocatalyst by integrating Pt with N-doped bimetallic oxide. The design leverages the synergistic effects between Pt's superior catalytic activity and electrical conductivity, and the tuneable surface chemistry, defect structure, and inherent stability of N-doped BMOs. Mn_2O_3 contributed mainly through redox mediation and peroxide decomposition, improving ORR selectivity and supporting moderate OER activity. NiO contributed to the enhancement of OER through electronic modification and conductivity, by forming NiOOH, a highly active species for OER. Nitrogen doping in this case led to a decrease in specific surface area; however, this doping introduced surface defects and electronic structure modifications that enhanced Pt anchoring, promoted uniform dispersion, and facilitated charge transfer at the catalyst/support interface. These led to a significantly increased ECSA and reduced overpotentials for both oxygen electrode reactions. Among different identified nitrogen species, the pyridinic-N and graphitic-N particularly decrease the ORR onset potential and lead to higher diffusion-limited current density, respectively. Pyridinic and quaternary nitrogen can also act as active sites for the OER. Nitrogen doping modifies the electronic structure of the Mn and Ni oxides, creating specific Mn–N or Ni–N bonds and active sites, which promote the absorption of intermediates critical for both oxygen electrode reactions. Electrochemical measurements confirmed marked improvements in ORR and OER performance compared to the undoped BMO counterpart, validating the effectiveness of the combined N doping and Pt deposition strategy. Pt/N–Mn_2O_3–NiO (1 : 1) (S3) also demonstrated excellent long-term catalytic durability due to stabilisation of Pt nanoparticles by BMO and prevention of their agglomeration, detachment, and Ostwald ripening; this underscores high structural and electrochemical stability of Pt/N–Mn_2O_3–NiO (1 : 1) (S3), a critical requirement for practical deployment in energy conversion systems such as metal–air batteries and regenerative fuel cells.

Conclusions

The sluggish kinetics of the ORR and OER, as well as the high cost of Pt, IrO_2, and RuO_2 catalysts, have been among the main reasons why fuel cells and unitised regenerative fuel cells have not yet been commercialised. In this work, three slightly modified synthesis procedures were employed to synthesise twelve nitrogen-doped and Pt-decorated materials (three sets of four catalysts). Their performance in catalysing oxygen reduction and evolution was tested in alkaline media. Among all tested materials, Pt/N–Mn_2O_3–NiO (1 : 1) (S3) which was synthesised *via* the solid-state preparation of binary metal oxides (S3) method showed the best performance with the highest achieved diffusion-limited current density of −4.98 mA cm^{-2} at 1800 rpm, the highest kinetic current density of −15.3 mA cm^{-2} and low Tafel slope of 75 mV dec^{-1} in ORR potential region, and overpotential of 0.56 V to reach benchmark current value of 10 mA cm^{-2} in OER mode. Pt/N–Mn_2O_3–NiO (1 : 1) (S3) showed good bifunctional performance with ΔE of 0.95 V, the second lowest ΔE of all tested materials. The catalytic performance of Pt/N–Mn_2O_3–NiO (1 : 1) (S3) proved to be comparable with the commercial 40 wt% Pt/C, although it should be noted that herein synthesised materials contain only 20 wt% of Pt, which makes them much cheaper to produce. Pt/N–Mn_2O_3–NiO (1 : 1) (S3) also showed remarkable stability during the 1000-cycle AST and 10 h switch test, much better than the commercial Pt/C tested in the author's previous work,[15] proving its performance and potential for application in alkaline fuel cells and unitised regenerative fuel cells.

Author contributions

Conceptualisation, B. Š. and A. B., investigation, K. G., D. M., Y. A., and G. S.; data curation K. G., D. M., Y. A.; writing—original draft preparation, K. G., D. M., Y. A., and G. S.; writing—review and editing, B. Š., D. M. F. S., A. B., and G. S.; visualisation, K. G., D. M., Y. A.; supervision, B. Š., D. M. F. S., and A. B.

Conflicts of interest

The authors declare that they have no known competing financial interests or personal relationships that could have appeared to influence the work reported in this paper.

Data availability

Data supporting this study has been included as part of the main manuscript and SI. The Supplementary Information file includes additional data, figures, and methodological details that support the findings presented in the main manuscript. See DOI: **https://doi.org/10.1039/d5dt01211b**.

Acknowledgements

This work was supported by the Ministry of Science, Technological Development and Innovation of the Republic of Serbia (contract no. 451-03-136/2025-03/200146 and 451-03-137/2025-03/200146) and by the Fundação para a Ciência e a

Tecnologia, FCT, Portugal (under contract LA/P/0095/2020, LaPMET, Laboratory of Physics for Materials and Emerging Technologies, and a Principal Researcher contract (2023.09426.CEECIND, https://doi.org/10.54499/2023.09426.CEECIND/CP2830/CT0021) in the scope of the Individual Call to Scientific Employment Stimulus – 6th Edition (D. M. F. S)).

References

1 Y. Wang, D. Y. C. Leung, J. Xuan and H. Wang, A review on unitized regenerative fuel cell technologies, part B: Unitized regenerative alkaline fuel cell, solid oxide fuel cell, and microfluidic fuel cell, *Renewable Sustainable Energy Rev.*, 2017, **75**, 775–795, DOI: 10.1016/j.rser.2016.11.054.

2 N. Mac Dowell, N. Sunny, N. Brandon, H. Herzog, A. Y. Ku, W. Maas, A. Ramirez, D. M. Reiner, G. N. Sant and N. Shah, The hydrogen economy: A pragmatic path forward, *Joule*, 2021, **5**, 2524–2529, DOI: 10.1016/j.joule.2021.09.014.

3 A. M. Oliveira, R. R. Beswick and Y. Yan, A green hydrogen economy for a renewable energy society, *Curr. Opin. Chem. Eng.*, 2021, **33**, 100701, DOI: 10.1016/j.coche.2021.100701.

4 L. Barreto, A. Makihira and K. Riahi, The hydrogen economy in the 21st century: A sustainable development scenario, *Int. J. Hydrogen Energy*, 2003, **28**, 267–284, DOI: 10.1016/S0360-3199(02)00074-5.

5 M. Ball and M. Weeda, The hydrogen economy - Vision or reality?, *Int. J. Hydrogen Energy*, 2015, **40**, 7903–7919, DOI: 10.1016/j.ijhydene.2015.04.032.

6 R. O'Hayre, S. Cha, W. Colella and F. B. Prinz, *Fuel Cell Fundamentals*, 2016. DOI: 10.1002/9781119191766.

7 T. Sadhasivam, K. Dhanabalan, S. H. Roh, T. H. Kim, K. W. Park, S. Jung, M. D. Kurkuri and H. Y. Jung, A comprehensive review on unitized regenerative fuel cells: Crucial challenges and developments, *Int. J. Hydrogen Energy*, 2017, **42**, 4415–4433, DOI: 10.1016/j.ijhydene.2016.10.140.

8 K. B. Ibrahim, M. C. Tsai, S. A. Chala, M. K. Berihun, A. W. Kahsay, T. A. Berhe, W. N. Su and B. J. Hwang, A review of transition metal-based bifunctional oxygen electrocatalysts, *J. Chin. Chem. Soc.*, 2019, **66**, 829–865, DOI: 10.1002/jccs.201900001.

9 K. Zhang and R. Zou, Advanced transition metal-based OER electrocatalysts: Current status, opportunities, and challenges, *Small*, 2021, **17**, 2100129, DOI: 10.1002/smll.202100129.

10 D. Mladenović, A. Mladenović, D. M. F. Santos, A. B. Yurtcan, Š. Miljanić, S. Mentus and B. Šljukić, Transition metal oxides for bifunctional ORR/OER electrocatalysis in unitized regenerative fuel cells, *J. Electroanal. Chem.*, 2023, **946**, 117709, DOI: 10.1016/j.jelechem.2023.117709.

11 G. Yusibova, J. M. Assafrei, K. Ping, J. Aruväli, P. Paiste, M. Käärik, J. Leis, H. M. Piirsoo, A. Tamm, A. Kikas, V. Kisand, P. Starkov and N. Kongi, Bimetallic metal-organic-framework-derived porous cobalt manganese oxide bifunctional oxygen electrocatalyst, *J. Electroanal. Chem.*, 2023, **930**, 117161, DOI: 10.1016/j.jelechem.2023.117161.

12 T. Zhao, Y. H. Wu, Z. R. Song, X. Wang, R. L. Yin, H. Xu, H. Cui, X. H. Cao and J. K. Gao, MOF-derived nitrogen-doped iron–nickel oxide carbon nanotubes as efficient oxygen electrocatalyst for long-life rechargeable zinc–air batteries, *Rare Met.*, 2023, **42**, 3326–3336, DOI: 10.1007/s12598-023-02415-9.

13 D. M. Morales, M. A. Kazakova, S. Dieckhöfer, A. G. Selyutin, G. V. Golubtsov, W. Schuhmann and J. Masa, Trimetallic Mn-Fe-Ni oxide nanoparticles supported on multi-walled carbon nanotubes as high-performance bifunctional ORR/OER electrocatalyst in alkaline media, *Adv. Funct. Mater.*, 2020, **30**, 1905992, DOI: 10.1002/adfm.201905992.

14 C. Shao, F. Liao, W. Zhu, Y. Zhang, M. Ma, J. Yang, K. Yin, M. Shao and B. Jiang, Carbon dots bridge NiO and Mn_2O_3 as highly efficient bifunctional oxygen electrocatalysts for rechargeable zinc-air batteries, *Appl. Surf. Sci.*, 2022, **596**, 153642, DOI: 10.1016/j.apsusc.2022.153642.

15 D. Mladenović, D. M. F. Santos, G. Bozkurt, G. S. P. Soylu, A. B. Yurtcan, Š. Miljanić and B. Šljukić, Tailoring metal-oxide-supported PtNi as bifunctional catalysts of superior activity and stability for unitised regenerative fuel cell applications, *Electrochem. Commun.*, 2021, **124**, 106963, DOI: 10.1016/j.elecom.2021.106963.

16 D. Mladenović, Y. Aykut, A. B. Yurtcan, G. S. P. Soylu, D. M. F. Santos, Š. Miljanić and B. Šljukić, Optimizing oxygen electrode bifunctionality with platinum and nickel nanoparticle-decorated nitrogen-doped binary metal oxides, *Processes*, 2024, **12**, 453, DOI: 10.3390/pr12030453.

17 W. Chen, J. Huang, J. Wei, D. Zhou, J. Cai, Z. Da He and Y. X. Chen, Origins of high onset overpotential of oxygen reduction reaction at Pt-based electrocatalysts: A mini review, *Electrochem. Commun.*, 2018, **96**, 71–76, DOI: 10.1016/j.elecom.2018.09.011.

18 N. M. Marković, T. J. Schmidt, V. Stamenković and P. N. Ross, Oxygen reduction reaction on Pt and Pt bimetallic surfaces: A selective review, *Fuel Cells*, 2001, **1**, 105–116, DOI: 10.1002/1615-6854(200107)1:2<105::aid-fuce105>3.3.co;2-0.

19 Y. Matsumoto and E. Sato, Electrocatalytic properties of transition metal oxides for oxygen evolution reaction, *Mater. Chem. Phys.*, 1986, **14**, 397–426, DOI: 10.1016/0254-0584(86)90045-3.

20 J. Pan, X. L. Tian, S. Zaman, Z. Dong, H. Liu, H. S. Park and B. Y. Xia, Recent progress on transition metal oxides as bifunctional catalysts for lithium-air and zinc-air batteries, *Batteries Supercaps*, 2019, **2**, 336–347, DOI: 10.1002/batt.201800082.

21 W. J. J. Stevens, V. Meynen, E. Bruijn, O. I. Lebedev, G. Van Tendeloo, P. Cool and E. F. Vansant, Mesoporous material formed by acidic hydrothermal assembly of silicalite-1 precursor nanoparticles in the absence of meso-templates, *Microporous Mesoporous Mater.*, 2008, **110**, 77–85, DOI: 10.1016/j.micromeso.2007.09.007.

22 L. Yao, Q. Liu, S. Mossin, D. Nielsen, M. Kong, L. Jiang, J. Yang, S. Ren and J. Wen, Promotional effects of nitrogen doping on catalytic performance over manganese-containing semi-coke catalysts for the NH_3-SCR at low tempera-

tures, *J. Hazard. Mater.*, 2020, **387**, 121704, DOI: 10.1016/j.jhazmat.2019.121704.
23 Y. Wan, W. Zhao, Y. Tang, L. Li, H. Wang, Y. Cui, J. Gu, Y. Li and J. Shi, Ni-Mn bi-metal oxide catalysts for the low temperature SCR removal of NO with NH_3, *Appl. Catal., B*, 2014, **148–149**, 114–122, DOI: 10.1016/j.apcatb.2013.10.049.
24 D. Y. Osadchii, A. I. Olivos-Suarez, A. V. Bavykina and J. Gascon, Revisiting nitrogen species in covalent triazine frameworks, *Langmuir*, 2017, **33**, 14278–14285, DOI: 10.1021/acs.langmuir.7b02929.
25 A. Öztürk and A. Bayrakçeken Yurtcan, Preparation and characterization of melamine-led nitrogen-doped carbon blacks at different pyrolysis temperatures, *J. Solid State Chem.*, 2021, **296**, 121972, DOI: 10.1016/j.jssc.2021.121972.
26 N. Zhou, N. Wang, Z. Wu and L. Li, Probing Active Sites on Metal-Free, Nitrogen-Doped Carbons for Oxygen Electroreduction: A Review, *Catalysts*, 2018, **8**, 509.
27 L. Qu, Y. Liu, J.-B. Baek and L. Dai, Nitrogen-Doped Graphene as Efficient Metal-Free Electrocatalyst for Oxygen Reduction in Fuel Cells, *ACS Nano*, 2010, **4**, 1321–1326.
28 K. Gong, F. Du, Z. Xia, M. Durstock and L. Dai, Nitrogen-Doped Carbon Nanotube Arrays with High Electrocatalytic Activity for Oxygen Reduction, *Science*, 2009, **323**, 760–764.
29 H. Zhang, H. Li, X. Zhang, S. Yu, S. Wang and G. Sun, Enhanced metal-support interaction of nitrogen-doped carbon supported Pt nanoparticles with high activity for electrocatalytic oxygen reduction reaction, *Carbon Neutrality*, 2025, **4**, 10.
30 X. Ning, Y. Li, J. Ming, Q. Wang, H. Wang, Y. Cao, F. Peng, Y. Yang and H. Yu, Electronic synergism of pyridinic- and graphitic-nitrogen on N-doped carbons for the oxygen reduction reaction, *Chem. Sci.*, 2019, **10**, 1589–1596.
31 C. C. L. McCrory, S. Jung, J. C. Peters and T. F. Jaramillo, Benchmarking heterogeneous electrocatalysts for the oxygen evolution reaction, *J. Am. Chem. Soc.*, 2013, **135**, 16977–16987, DOI: 10.1021/ja407115p.
32 R. Kumar, A. Agrawal, R. K. Nagarale and A. Sharma, High performance supercapacitors from novel metal-doped ceria-decorated aminated graphene, *J. Phys. Chem. C*, 2016, **120**, 3107–3116, DOI: 10.1021/acs.jpcc.5b09062.
33 J. Ustarroz, B. Geboes, H. Vanrompay, K. Sentosun, S. Bals, T. Breugelmans and A. Hubin, Electrodeposition of highly porous Pt nanoparticles studied by quantitative 3D electron tomography: Influence of growth mechanisms and potential cycling on the active surface area, *ACS Appl. Mater. Interfaces*, 2017, **9**, 16168–16177, DOI: 10.1021/acsami.7b01619.
34 M. A. Qadeer, X. Zhang, M. A. Farid, M. Tanveer, Y. Yan, S. Du, Z. F. Huang, M. Tahir and J. J. Zou, A review on fundamentals for designing hydrogen evolution electrocatalyst, *J. Power Sources*, 2024, **613**, 234856, DOI: 10.1016/J.JPOWSOUR.2024.234856.
35 A. Mladenović, Y. Aykut, D. Mladenović, D. M. F. Santos, A. Bayrakçeken, G. S. P. Soylu and B. Šljukić, Platinum on nitrogen-doped Mn_2O_3–NiO as a bifunctional electrocatalyst for air cathodes, *J. Phys. Chem. Solids*, 2025, **199**, 112575, DOI: 10.1016/J.JPCS.2025.112575.
36 M. A. R. Khan, M. S. Al Mamun and M. H. Ara, Review on platinum nanoparticles: Synthesis, characterization, and applications, *Microchem. J.*, 2021, **171**, 106840, DOI: 10.1016/j.microc.2021.106840.
37 H. R. Q. Jhong, F. R. Brushett and P. J. A. Kenis, The effects of catalyst layer deposition methodology on electrode performance, *Adv. Energy Mater.*, 2013, **3**, 589–599, DOI: 10.1002/aenm.201200759.
38 J. R. Swierk, S. Klaus, L. Trotochaud, A. T. Bell and T. D. Tilley, Electrochemical study of the energetics of the oxygen evolution reaction at Nickel Iron (Oxy)Hydroxide Catalysts, *J. Phys. Chem. C*, 2015, **119**, 19022–19029, DOI: 10.1021/acs.jpcc.5b05861.
39 G. J. Brug, A. L. G. van den Eeden, M. Sluyters-Rehbach and J. H. Sluyters, The analysis of electrode impedances complicated by the presence of a constant phase element, *J. Electroanal. Chem.*, 1984, **176**, 275–295, DOI: 10.1016/S0022-0728(84)80324-1.
40 Z. Qiu, Y. Ma, G. A. Niklasson and T. Edvinsson, An electrochemical impedance study of alkaline water splitting using Fe doped NiO nanosheets, *PhysChem*, 2021, **1**, 69–81, DOI: 10.3390/physchem1010005.
41 Z. Zhang, X. Liang, J. Li, J. Qian, Y. Liu, S. Yang, Y. Wang, D. Gao and D. Xue, Interfacial engineering of $NiO/NiCo_2O_4$ porous nanofibers as efficient bifunctional catalysts for rechargeable Zinc-air batteries, *ACS Appl. Mater. Interfaces*, 2020, **12**, 21661–21669, DOI: 10.1021/acsami.0c03672.
42 X. F. Lu, Y. Chen, S. Wang, S. Gao and X. W. Lou, Interfacing manganese oxide and cobalt in porous graphitic carbon polyhedrons boosts oxygen electrocatalysis for Zn–air batteries, *Adv. Mater.*, 2019, **31**, 1902339, DOI: 10.1002/adma.201902339.
43 X. Xiao, W. Zhang, H. Zhao, L. Li, P. Deng, Y. Wu, S. Luo and B. Chen, Ultrathin amorphous MnO_2 modified prawn shells-derived porous carbon towards robust oxygen electrocatalyst for rechargeable Zn-air battery, *Ceram. Int.*, 2022, **48**, 6506–6511, DOI: 10.1016/j.ceramint.2021.11.195.
44 M. He, X. Jin, F. Chen, J. Chen, J. Min, H. Duan, X. Kuang, J. Li, Z. Wu and J. Li, Synergistic effect of Mn^{3+} and oxygen vacancy on the bifunctional oxygen electrocatalytic performance of MnOX/CNTs composites, *J. Alloys Compd.*, 2023, **933**, 167728, DOI: 10.1016/j.jallcom.2022.167728.
45 A. Paul, T. A. R. Silva, M. M. A. Soliman, J. Karačić, B. Šljukić, E. C. B. A. Alegria, R. A. Khan, M. F. C. Guedes da Silva and A. J. L. Pombeiro, Benzimidazole Schiff base copper(II) complexes as catalysts for environmental and energy applications: VOC oxidation, oxygen reduction and water splitting reactions, *Int. J. Hydrogen Energy*, 2022, **47**, 23175–23190, DOI: 10.1016/j.ijhydene.2022.04.271.
46 K. Kisand, A. Sarapuu, A. Kikas, V. Kisand, M. Rähn, A. Treshchalov, M. Käärik, H. M. Piirsoo, J. Aruväli, P. Paiste, J. Leis, V. Sammelselg, A. Tamm and K. Tammeveski, Bifunctional multi-metallic nitrogen-doped nanocarbon catalysts derived from 5-methylresorcinol, *Electrochem. Commun.*, 2021, **124**, 106932, DOI: 10.1016/j.elecom.2021.106932.